MDPI

Article

Research Progress on Development of PVP-Ag-Doped LaMnO$_3$ Composites for Methyl Orange Degradation

Adina Căta [1], Madalina-Gabriela Ivanovici [1,2], Paula Svera [1], Ioana Maria Carmen Ienașcu [1,3] and Paula Sfirloaga [1,*]

[1] National Institute of Research and Development for Electrochemistry and Condensed Matter, 144 Dr. A. P. Podeanu, 300569 Timişoara, Romania; adina.cata@yahoo.com (A.C.); ivanovicigabriela11@yahoo.com (M.-G.I.); paulasvera@gmail.com (P.S.); imcienascu@yahoo.com (I.M.C.I.)

[2] Faculty of Industrial Chemistry and Environmental Engineering, Politehnica University of Timisoara, Bv. Vasile Parvan No. 6, 300223 Timisoara, Romania

[3] Department of Pharmaceutical Sciences, Faculty of Pharmacy, "Vasile Goldiș" Western University of Arad, 86 Liviu Rebreanu, 310045 Arad, Romania

[*] Correspondence: paulasfirloaga@gmail.com

Abstract: Water pollution caused by emerging contaminants is increasing due to rising urbanization, industrialization, and agriculture production; therefore, new materials with high efficiency for wastewater decontamination are needed. A perovskite material based on 1% Ag-doped LaMnO$_3$ synthesized through a sol–gel technique was combined with PVP in a 1:10 (w/w) ratio and subjected to different temperature and microwave conditions at various time intervals. The composite materials were obtained as thin films (S1, S2) or powders (S3) and were analyzed by modern techniques. The SEM analysis showed strongly agglomerated, asymmetric formations for the S1, S2 materials; as for the S3 composite, irregularly shaped grains of perovskite were deposited on the polymer surface. Small, round formations across the surface, mainly organized as clusters with conic/square-shaped particles and observed asperity on top, were highlighted by AFM images. The XRD spectra confirmed the presence of both the perovskite and PVP phases, and the crystallite size of the materials was determined to be in the range of 33–43 nm. The structural analyses, FT-IR, and Raman spectroscopy proved the interactions between the perovskite and the polymer, which led to novel composite materials. The different methods used for the synthesis of the new materials influenced their features and behavior. Moreover, the composites were successfully tested for methyl orange (MO) elimination from an acidic aqueous solution in dark conditions, with fast and complete (>95%) MO degradation at pH = 2.

Keywords: LaMnO$_3$:Ag perovskite; PVP–perovskite composites; morphology; MO degradation

1. Introduction

Due to the rapid growth rate of the global population over the last few centuries, industrialization and urbanization have highly increased, leading to a major impact on water pollution. Water contaminants cause negative effects on human health; many respiratory and allergic conditions, even cancer, can be related to water pollution [1]. Organic contaminants, like dyes, petrochemicals, or drugs, represent important pollution sources [2]; thus, many investigations have been conducted in order to develop techniques or materials that can be used for the decontamination of wastewater. The classical treatments of wastewater

include adsorption, membrane filtration, sedimentation techniques, and biological methods. These solve the problem to a certain extent, but they come with a number of disadvantages, such as large volumes of solvent for washing the adsorbents, severe secondary pollution, high startup and process costs, and prolonged time [3].

Advanced oxidation processes (AOPs) represent an alternative to the conventional techniques used for water decontamination, and their recent popularity for the efficient removal of organic pollutants by the production of highly reactive oxygen species is also due to the great range of applications they have due to their strong oxidation capacities and short reaction times, with fewer secondary pollutants. However, their relatively high operational costs compared to more economical conventional technologies, such as biological treatments, are the main drawback of AOPs [4]. Among the AOPs, heterogeneous catalyst-assisted oxidation is one of the preferred techniques for eliminating pollutants from wastewater due to its simplicity, flexibility, and good cost–efficiency ratio [5,6]. Various photocatalytic active materials, such as metals, metal oxides, perovskites, polymers, graphitic carbon nitrides, and organic frameworks, have been employed for this kind of application [5].

In recent years, due to their favorable structural, optical, and electronic properties, perovskite nanomaterials have gained interest in terms of their application in the catalytic and photocatalytic breakdown of organic pollutants, and considerable efforts have been employed to improve their performance and to overcome the issues regarding the separation and recycling of perovskites [5,6]. While unmodified single-phase perovskites may not provide sufficient photocatalytic efficiency for the degradation of organic pollutants, different strategies, such as ion doping and structural modifications, have been proposed to improve their performance, allowing for the customization of their specific properties [7].

Thus, simple and doped perovskites have been synthesized and tested for their ability to act as catalysts for contaminant removal. For instance, good results were obtained when using $LaFeO_3$ [8,9], $LaMnO_3$ [10], $BiFeO_3$ [11], and $BaBiO_3$ [12] perovskites for the degradation of organic compounds such as phenol [9], erythrosine [8], eriochrome black T [8], methyl orange [10], doxorubicin [11], and rhodamine B [12] under UV [11], visible [8,9,12], or solar [10] irradiation. Doping is a well-known approach to improve the oxidative properties of perovskites, as observed in the case of Gd-doped $MTiO_3$ (M = Co, Cu, and Ni) [13] and La- and Cr-doped $SrTiO_3$ [14] perovskites. In the case of $LaFeO_3$ nanostructures, natural capping agents such as corn, starch, and rice have been used to increase the degradation efficiency of some organic dyes under visible light [8].

Another way to enhance the photocatalytic activity of perovskites is to use them in the form of composites. Thus, perovskites have been combined with various semiconductors, i.e., carbon, titanium dioxide, graphene oxide, montmorillonite, silver phosphate, cadmium selenide, copper oxide, and zinc oxide [5]. Also, organic–inorganic hybrid perovskite materials have been tested both as materials for the fabrication of high-performance photovoltaic cells [15] and as photocatalysts for the degradation of organic contaminants [15]. Perovskite–organic material composites display complex structures, which can result in a broader contact surface area and extended reactive sites targeting heightened catalysis processes [16]. Organic materials such as polymers also have a "passive" role wherein they serve as hosts for encapsulating and fixing the nano-catalyst in their matrix [17,18]. Multiple emerging properties are another intrinsic consequence of their synergetic combination and kinetically controlled electrochemical reactions; strengthened resistance to external aggressive stimuli (high temperature, humidity, polar solvents, electromagnetic radiation), the creation of filters for the selective passage of some species, hindered particle agglomeration, and even luminescent properties can be specified as some of their attributes [16–20].

Novel polymer–perovskite composites composed of carbon nitride and different types of perovskites ($BaTiO_3$, $SrTiO_3$, and $CaTiO_3$) have been successfully developed for photocatalytic degradation of methyl orange, bisphenol A, and Rhodamine B [16,21,22]. Perovskites such as $Nd_{0.9}TiO_3$ and $LaTiO_3$, each of them immobilized separately on polymers based on TMPTA, Ebecryl 40, PETIA, and SR-610, showed significant photodegradation of acid black dye, which was even higher for the hybrid materials of perovskite- and TMPTA-based polymers when compared to the universal TiO_2 hybridized with TMPTA based polymer [23].

Polyvinylpyrrolidone (PVP) is a water-soluble, non-toxic, non-ionic polymer containing a strongly hydrophilic component (the pyrrolidone moiety) and a considerable hydrophobic group (the alkyl group). It is widely utilized in nanoparticle synthesis as a great stabilizer [24] and also as a carrier to support photocatalysts [25]. PVP was used in the synthesis of the $Bi_5O_7Br_xI_{1-x}$ nanomaterial and proved to act as a crystal surface inhibitor that reduced the surface tension, regulated crystal growth, and promoted the directional nucleation of the photocatalytic nanomaterial. The novel solid solution of the catalyst demonstrated high degradation efficiency towards levofloxacin under visible light [26]. The dispersibility and stability of δ-CsPbI3 microcrystals in water were enhanced by passivating the microcrystal with PVP. The obtained material was used for the complete visible light photodegradation of some organic dyes and was maintained in water for at least 30 days without obvious deterioration [27]. Also, recent studies have reported the use of PVP as a capping agent [25,28], dispersing agent and wettability regulator [29], stabilizing agent [30], or surface stabilizer and nanoparticle dispersant [31] to obtain various composite materials which have been successfully applied for the degradation of some organic contaminants. Considering this, we considered PVP a potential suitable polymeric matrix candidate for the preparation of composite materials.

This study reports the development of some new polymer/perovskite composites based on polyvinylpyrrolidone and a previously synthesized perovskite 1% Ag-doped $LaMnO_3$. Three different synthesis procedures were used, keeping the same mass ratio between perovskite and polymer. The obtained materials were analyzed by different analytical techniques (XRD, SEM, FT-IR, Raman) in order to evaluate whether the method of obtaining them would influence their physico-chemical properties. Furthermore, the behavior and applicability of these composite materials in the degradation of some organic pollutants in aqueous media was evaluated using methyl orange as a representative colored pollutant. The current research continues our previously reported experiments [10] regarding the investigation of the catalytic and photocatalytic activity of undoped and 1% Ag-, Pd, and Y-doped $LaMnO_3$. Ag-doped $LaMnO_3$ led to a better performance regarding MO degradation under dark conditions in comparison with the other doped materials, so it was chosen as a key material for the development of the new composite materials.

2. Materials and Methods

2.1. Materials and Reagents

The perovskite material (1% Ag-doped $LaMnO_3$) was previously synthesized through a sol–gel technique and properly characterized [10]. Polyvinylpyrrolidone (PVP), Mw ~40,000 g/mol, with a purity of ≥95%, was obtained from Sigma-Aldrich (St. Louis, MO, USA). Methyl orange (MO) and nitric acid 65% were obtained from Merck (St. Louis, MO, USA). The double-distilled water was produced in the laboratory.

2.2. Synthesis of PVP-Perovskite Composites

In this study, some polymer–perovskite materials in a PVP:perovskite ratio of 10:1 (*w/w*) were prepared using the following three methods:

S1. PVP was separately dissolved in 5 mL of double-distilled water under stirring at room temperature. The perovskite was then incorporated into the PVP solution under stirring, and the resulting mixture was sealed in a 50 mL Teflon-lined stainless-steel reactor and kept at 150 °C for 4 h in a hot-air oven. The reactor was then allowed to cool, and the resulting viscous mixture was cast into thin films 2–5 mm in thickness on a flat surface (polypropylene film), which were dried at room temperature for 12 h. For catalysis experiments and morpho-structural characterization, powdered films were used.

S2. PVP was separately dissolved in 5 mL of double-distilled water under stirring at room temperature. The perovskite was then incorporated into the PVP solution under stirring, and the resulting mixture was sealed in a 60 mL high-pressure Teflon reactor (DAP-60K, Berghof Products + Instruments GmbH, Eningen, Germany) and kept at 150 °C and a microwave power 800 W for 30 min using the microwave pressure digestion system speedwave MWS-2 (Berghof Products + Instruments GmbH, Eningen, Germany). The mixture was then concentrated until an optimum viscosity was reached in order to cast it into thin films 2–5 mm in thickness on a flat surface (polypropylene film), which were dried at room temperature for 12 h. For catalysis experiments and morpho-structural characterization, powdered films were used.

S3. The two solids (PVP and perovskite) were blended until a homogenous mixture was obtained. The mixture was then kept in a hot-air oven at 200 °C for 8 h in a crucible. The resulting powder was kept in an exicator until further analyses.

2.3. Characterization of Composite Materials

The crystal structures and phases of the PVP-perovskite composites were studied via X-ray diffraction (XRD). XRD patterns were collected on a X'Pert Pro MPD-type diffractometer (PANalytical, Almelo, The Netherlands) with Cu-Kα radiation (λ = 1.54060 Å). The XRD data were collected in the 2θ range from 15 to 80° with a collection time of 0.2 sec/step. The ATR-FT-IR spectra were acquired with a Bruker Vertex 70 spectrometer (Bruker Optik GmbH, Rosenheim, Germany) equipped with a Platinium ATR unit, Bruker Diamond A225/Q.1, in the range of 4000–600 cm^{-1}. The morphology of the samples was registered using a scanning electron microscope EmCrafts CUBE II (EmCrafts Co. Ltd., Gwangju-si, Republic of Korea) in high vacuum mode. The Raman spectra were obtained with a Shamrock 500i Spectrograph (Andor Technology Ltd., Belfast, UK) at room temperature using 514 nm laser excitation. AFM analyses were accomplished with Nanonics MultiView 2000 scanner (Nanonics, Jerusalem, Israel) in intermittent mode at room temperature using silicone-Cr-coated probes with tip radii of 20 nm and resonance frequencies of 30–40 kHz.

2.4. Degradation of Methyl Orange

This investigation was conducted to assess the application of synthesized materials for the elimination of colored organic compounds as a way to validate the materials' potential for degradation of many possible pollutants from aqueous media. Methyl orange (MO) was used as a representative colored pollutant. The degradation experiments involved the use of acidic suspensions consisting of MO aqueous solution and PVP-perovskite composites, which represent the reaction environment where the degradation reaction takes place. Each experimental test was conducted with 20 mL of MO aqueous solution at a concentration of 12 ppm and with the test material at a 500 ppm concentration, which were continuously stirred for a period of 2 h. The acidity of the MO aqueous solution was adjusted using 0.1 M HNO$_3$ aqueous solution prepared from nitric acid 65%. The test materials are represented by the S1, S2, and S3 samples, and each of them was separately studied in the aforementioned suspensions at three different pH values: 2, 3, and 4, respectively. Two more reference tests were performed with the solution only and with the solution

mixed with the polymer (polyvinylpyrrolidone-PVP) at pH = 2 using the same volume and concentration as the MO solution and a concentration of 454.5 ppm for PVP. Additionally, one more experiment was conducted using the same amount and concentration of MO solution adjusted to a pH between 2 and 3, along with the S3 sample, for a period of 4 h.

The elimination of MO was monitored by measuring the MO solution absorbance in the visible range for the 2 h experiments and in the UV-VIS range for the 4 h experiment, starting from the moment of the test material's addition to the MO solution and lasting for the entire period of the experiment. The absorbance was analyzed as follows: small volumes of solution were separated from the reaction mixture by centrifugation, and then the supernatant was added in a quartz cuvette optically connected to a UV-VIS spectrometer (Jaz spectrometer, modular and portable type from Ocean Optics) and to a light source (LS-1 tungsten halogen light source from Ocean Optics). This procedure was used to monitor the decrease in color through the decrease in absorbance intensity, and the effect of the tested materials in this application was assessed by calculating the discoloration efficiency (D_{eff}, %) using the well-known formula below:

$$D_{eff}(\%) = \frac{A_t - A_0}{A_0} \times 100 \tag{1}$$

In the mentioned equation, A_t stands for recorded absorbance at time t and A_0 refers to the first measured absorbance during the discoloration reaction. A schematic representation of the as-described experimental method is illustrated in Figure 1.
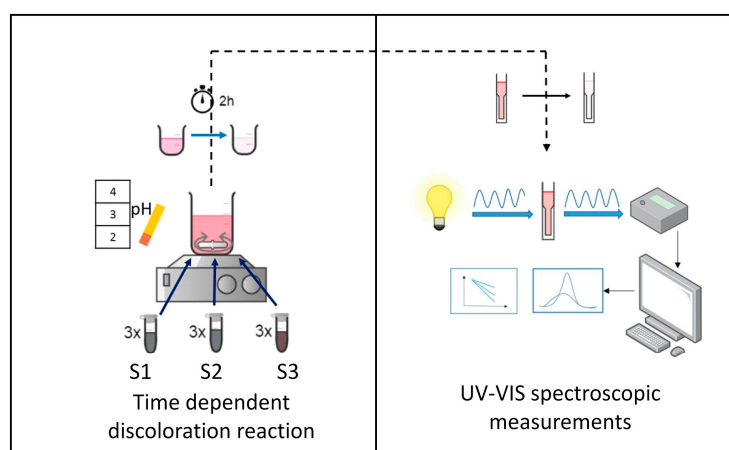

Figure 1. Schematic representation of experimental approach for evaluation of MO degradation assisted by PVP-perovskite composites.

3. Results and Discussion

3.1. XRD Analysis

The XRD characteristics of the prepared samples are shown in Figure 2. The unit cell parameters of PVP–perovskite composites, as well as the sizes of the crystallites, were obtained using the Rietveld refinement technique with High Score Plus software version 2.2b (2.2.2). The results obtained from the X-ray diffraction spectra analysis were correlated with the JCPDS database under reference number (01–072–0840), which includes orthorhombic crystal geometry and a Pnma space group. The crystallographic major peaks at the diffraction angles of 2θ = 22.9, 32.8, 40.4, 47.1, 53.0, 58.4, 58.8, and 68.7° corresponded to the (020), (121), (220), (202), (141), (321), (242), and (402) reflections of the perovskite phase. The crystallite size of the materials was calculated from the Scherrer equation and was found to be 38 nm (S1), 43 nm (S2), and 33 nm (S3). Moreover, the XRD patterns of S1

and S2 composites showed peaks corresponding to polyvinylpyrrolidone at the 21 theta, as shown with an asterisk in Figure 2.
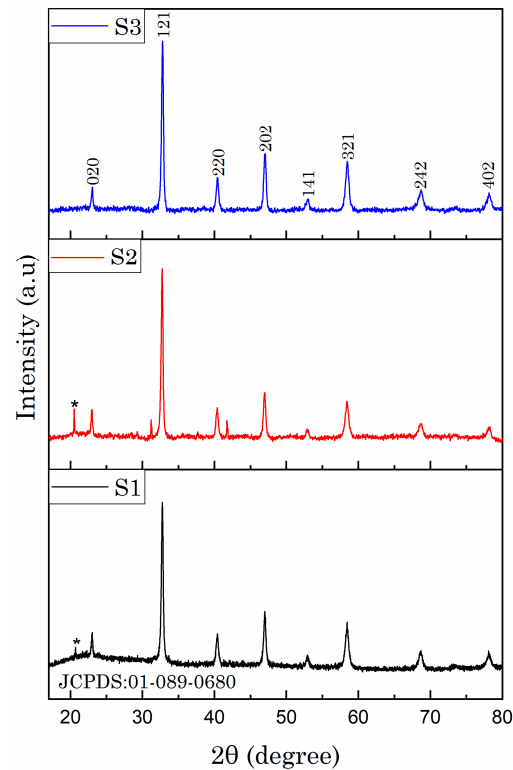

Figure 2. X-ray diffractograms for samples S1, S2, and S3.

3.2. SEM Analysis

Figure 3 presents the images obtained by scanning electron microscopy for the studied materials. In order to conduct a comparative study between the three types of obtained materials, they were analyzed under similar conditions: working mode—high vacuum, acceleration voltage—15 kV, and magnification—3000x. In this context, the morphological analysis of the surface highlighted that the synthesized materials were strongly agglomerated in asymmetric formations in the case of samples S1 and S2, while in the case of the S3 composite, the qualitative study showed that the perovskite material was deposited on the polymer in the form of irregular shaped grains. Moreover, EDX mapping for the 1% Ag-doped $LaMnO_3$ compound has been previously reported [10], where the purity of the material, the presence of the expected level of dopant, and the uniform distribution of the component elements were highlighted.
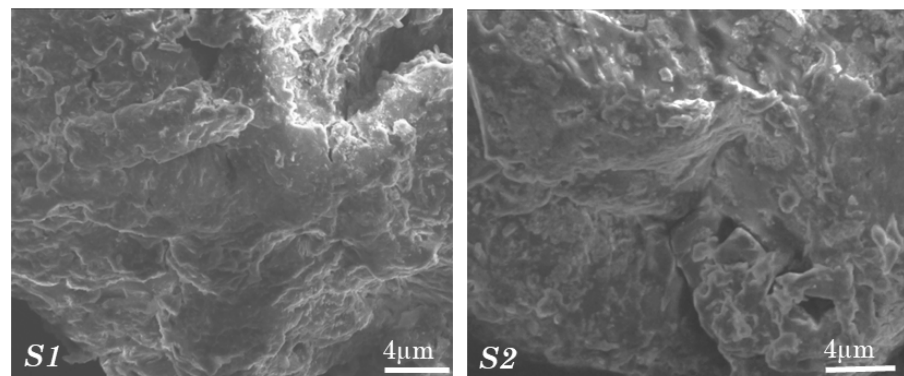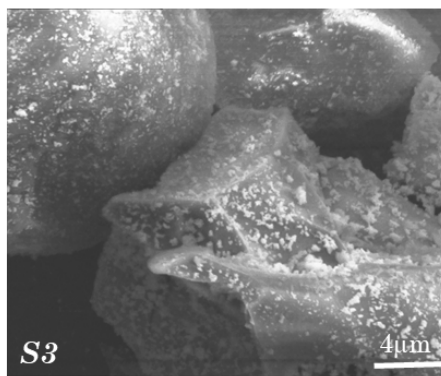

Figure 3. *Cont.*

Figure 3. The SEM images obtained for composites S1, S2, and S3.

3.3. FT-IR Analysis

The ATR-FT-IR spectra recorded for composite materials S1, S2 and S3 compared to the spectrum of pure PVP are presented in Figure 4.
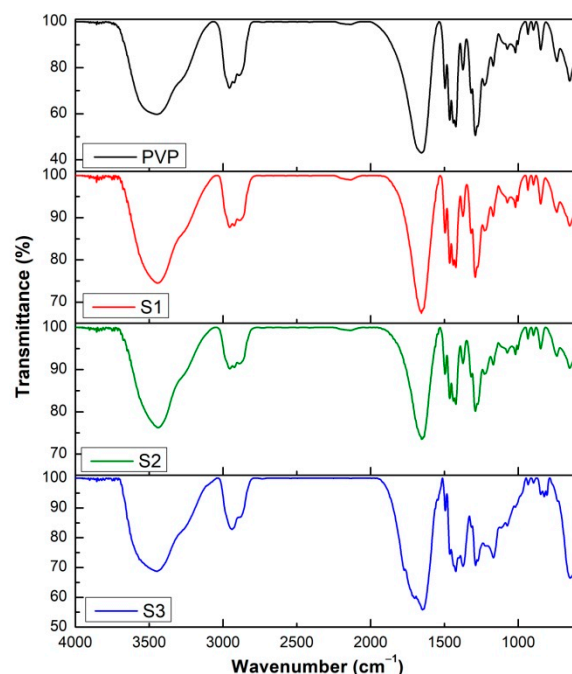

Figure 4. The FT-IR spectra of pure PVP and PVP–perovskite composites (S1, S2, S3).

The FT-IR spectra of pure PVP show the following important absorption bands at 3435 cm^{-1}, 2951 cm^{-1}, 1493−1421 cm^{-1}, and 1286 cm^{-1}, which can be assigned to O-H stretching, asymmetric C−H$_2$ stretching [24,32], C−H$_2$ deformations [33], and C–N bending vibration in the pyrrolidone structure [34], respectively.

Another strong absorption band located at 1651 cm^{-1} can be attributed to the C=O stretching vibration in the pyrrolidone group [24,32,34,35] and, as other authors have, to the amide I band of pyrrolidone [33].

Thus, if we compare the FT-IR spectra of PVP alone with the spectra of the composite materials, it can be observed that the C-H stretching vibration peaks blue-shifted from 2951 cm^{-1} (PVP) to 2953 cm^{-1} for samples S1 and S2, but for sample S3, no change was observed. Changes can also be detected for the broad band corresponding to O-H stretching vibration, which red-shifted from 3435 cm^{-1} (PVP) to 3414 cm^{-1} (S1), 3424 cm^{-1} (S2), and 3420 cm^{-1} (S3) in the composite materials. The C=O stretching band shifted from 1651 cm^{-1} to lower wavenumbers for two of the composite materials (1647 cm^{-1} for sample S1 and

1649 cm^{-1} for sample S2) and to a higher wavenumber (1655 cm^{-1}) for sample S3. This shift can be attributed to the coordination phenomenon among metallic species and carbonyl oxygen from PVP [35–37].

In the FT-IR spectra of the S3 composite material, compared to neat PVP, new bands (1520–1560 cm^{-1}, 1770 cm^{-1}) can be observed. This can be explained based on the different treatment. The S3 was obtained in more drastic conditions (8 h at 200 °C) compared to S1 and S2; thus, this composite material was no longer soluble. It was proven that, above 150°C, PVP suffers thermal densification as a result of cross-linking [38]. However, the FTIR spectra of soluble and cross-linked PVP were quite similar. The position and intensity of the carbonyl group remained the same, and only the intensity of the CH bond relative to C=O was reduced [39].

Borodko et al. [39] studied the in situ transformation of pure PVP in the temperature range of 25–400 °C (heating rate 2 deg/min) in H$_2$ atmosphere with the FTIR-DRIFT technique. It was concluded that, probably, the pyrrolidone rings are stable in the 25–400 °C range, and that decomposition and cross-linking happen generally in the backbone chain, with no evidence of ring opening being established.

In oxidizing environments (O$_2$ atmosphere), degradation of PVP starts around 100 °C, and the band of the carbonyl group moves to higher wavenumbers (1775 cm^{-1}, 1714 cm^{-1}), which can be assigned to the appearance of aliphatic ketones. Moreover, extra evidence of backbone dehydrogenation is the appearance of bands between 1590 and 1610 cm^{-1} allocated to the C=C stretch of a polyene sequence [40].

However, the spectra of the composite materials retain the main functional groups of the host polymer; thus, some differences regarding the position and intensity of the absorption bands corresponding to PVP are obvious, proving the interaction between PVP and perovskite, which leads to novel composite materials.

3.4. Raman Analysis

Due to the phenomenon of high fluorescence, the specific bands of the samples were difficult to distinguish, so multiple short acquisitions were used to obtain clearer Raman spectra of the analyzed materials (Figure 5).
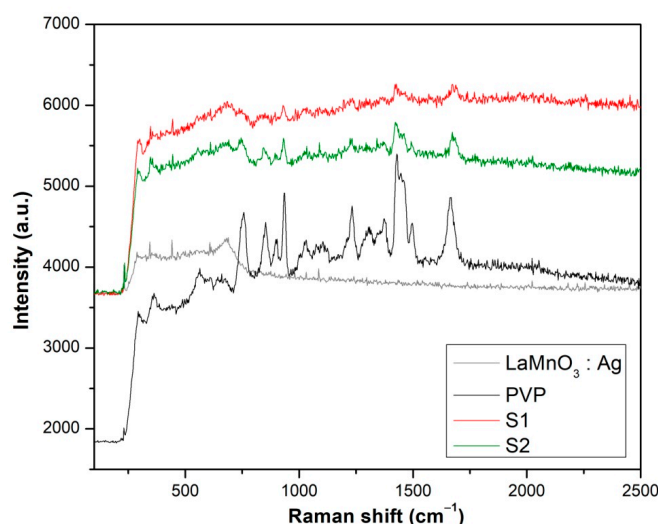

Figure 5. Raman spectra of pure PVP, LaMnO$_3$:Ag, and PVP–perovskite composites (S1, S2).

The PVP-specific bands are located in the Raman spectra at 300, 363, 562, 662, 756, 856, 903, 937, 1030, 1104, 1237, 1312, 1378, 1432, 1474 (shoulder), 1512, and 1665 cm^{-1}. The 1665 cm^{-1} band corresponds to the vibration of C=O bond, while 1312, 1378, 1432, and 1474 cm^{-1} are specific to the CH$_2$ bending [41]. The 1512 cm^{-1} band can be assigned

to the C–N bond [41]. Generally, the bands below 1000 cm^{-1} can be attributed to the vibrations of the C–C bonds, but the band at 562 cm^{-1} belongs to the N–C=O bending vibration [39]. However, in the presence of Ag or other metals, the PVP does not show any particular additional bands, the main difference being the aspect of the whole spectra [42]. Still, small shifts referring to the C=O–M (M = metal) may be present if the fluorescence is not overwhelming [39]. Borodko et al. [39] highlighted the importance of the heating temperature during analysis, resulting in spectral changes.

The Raman spectra of the composite materials (S1, S2) show specific bands of the two components [41,43], PVP and perovskite, as presented in Figure 5. It is obvious that many bands actually overlap, since there are bands in the same area originating from both PVP and perovskite. However, the difference between the S1 and S2 samples is mainly due to the preparation methods employed. The changes in the spectra of the composite materials are manifested through band shifts as well as band shape, with the most important differences being observed for the vibration of the C=O bond (1665 cm^{-1} for PVP, 1672 cm^{-1} for S1 and S2), the C–N bond (1512 cm^{-1} for PVP, 1499 cm^{-1} for S1, and 1492 cm^{-1} for S2), and the N–C=O bending vibration (562 cm^{-1} for PVP, 555 cm^{-1} for S1, and 554 for S2). All these shifts prove the interactions between the components in the newly obtained composite materials.

In addition, attempts were made regarding the analysis of sample S3 and PVP treated at 200 °C. Unlike samples S1 and S2, S3 was obtained under more drastic thermal conditions (8 h at 200 °C). It seems that during this prolonged heat treatment, PVP may undergo degradation/thermal densification as a result of cross-linking processes becoming insoluble, as we already mentioned in Section 3.3, *FT-IR analysis*. The appearance of higher fluorescence in the case of sample S3 was probably due to the transformations that PVP underwent during the heat treatment. The fluorescence of PVP has also been mentioned by other authors. Sudewi et al. [44] reported the synthesis of fluorescent polyvinylpyrrolidone-passivated iron oxide quantum dots using a hydrothermal reaction for 12 h at 200 °C. They used PVP for passivation and to obtain fluorescent properties of the developed materials, with higher amounts of PVP leading to increased fluorescence.

However, the temperature to which both samples S3 and PVP were subjected for treatment, 200 °C, substantially increased the florescence effect in the Raman spectra, making it impossible to obtain a clear spectrum. The cause of the encountered problem was the wavelength of the laser excitation source. The importance of the laser excitation wavelength in the case of samples with a tendency towards higher fluorescence has been mentioned in many works [45,46]. The anisotropy distribution of luminescent centers, which, in our case, were the Mn atoms originating from the LaMnO$_3$:Ag, may also induce variations in the intensity of polarized luminescence with variations in the luminescent intensity. The main role in the changes that take place in Raman spectra is played by the different synthesis conditions of the materials, with both the method and temperature having impacts which resulted in Raman changes. In addition, the morphology may also impact the Raman spectra, as reported by Berthou et al. [47], which is also in correlation with our results obtained through SEM.

3.5. AFM Analysis

AFM analysis was performed for samples S1 and S2, revealing the roughness data extracted from the obtained images. Several attempts were made in the case of sample S3; however, due to the different surface aspect along with the higher asperity, it was impossible to perform AFM analysis successfully. The different aspect of sample S3 in comparison to sample S1 and sample S2 is visible in the SEM images. The values calculated from AFM images (average roughness (Sa), mean square root roughness (Sq), maximum peak height (Sp), maximum valley depth (Sv), maximum peak-to-valley height (Sy), surface kurtosis (Sku), and surface skewness (Ssk)) are shown in Table 1.

Table 1. Values obtained from AFM analysis.

Sample Name	Ironed Area (μm^2)	Sa (μm)	Sq (μm)	Sp (μm)	Sv (μm)	Sy (μm)	Sku	Ssk
S1	458.087	0.1125	0.1453	0.5827	−0.5283	1.111	3.6416	0.1855
S2	439.306	0.0954	0.1233	0.5335	−0.5455	1.079	3.6217	0.1102

From the obtained data, sample S1 shows the higher roughness (Sa = 0.1125 μm and Sq = 0.1453 μm). The Sp and Sv values refer to the lowest pits and highest peaks registered in the analyzed area, which together provide the Sy value, which is indicated in the 3D images as Z. In both samples, the Sp values were around 0.5 μm, whereas the Sv values were around −0.5 μm. Ssk values provide information related to the number of high peaks and deep valleys, which can also indicate the homogeneity of the layer. For both samples, the Ssk value was positive, indicating the dominance of peaks over valleys. The Sku value >3 indicated the preponderance of steep heights in both cases.

The samples exhibit similar aspects (Figures 6–9), with small round formations across the surface, which are mainly organized in form of clusters. The profile analysis of the selected areas also provides insight into the surface details, revealing round formations with sizes of 1–3 μm and variable height between 300 and 600 nm. According to the profile analysis, in the case of sample S1, the shape of the particles was more conic, whereas in case of sample S2, the shape was more squared, with observed asperity on top. This type of asperity led to lower rugosity results as well. Since the rugosity data were obtained by taking into consideration the entire analyzed surface, the results also consider the most prevalent heights and valleys of the sample's surface. For this reason, the profiles of selected areas provided additional information that gave us more insight into the absorption process. As related by Rahimi et al. [48], the correlation between the surface area and rugosity is inversely proportional, since, with the increase in the surface area, the rugosity decreases. The observed asperity in the case of sample S2 may be the cause of the difference in the absorbance results. There were portions on the top of the S2 surface where the asperities were ~50 nm, making it an ideal trap for ions. Due to the presence of smaller asperities in limited areas, increased absorbance values were registered in the case of sample S2.

(**a**)

(**b**)
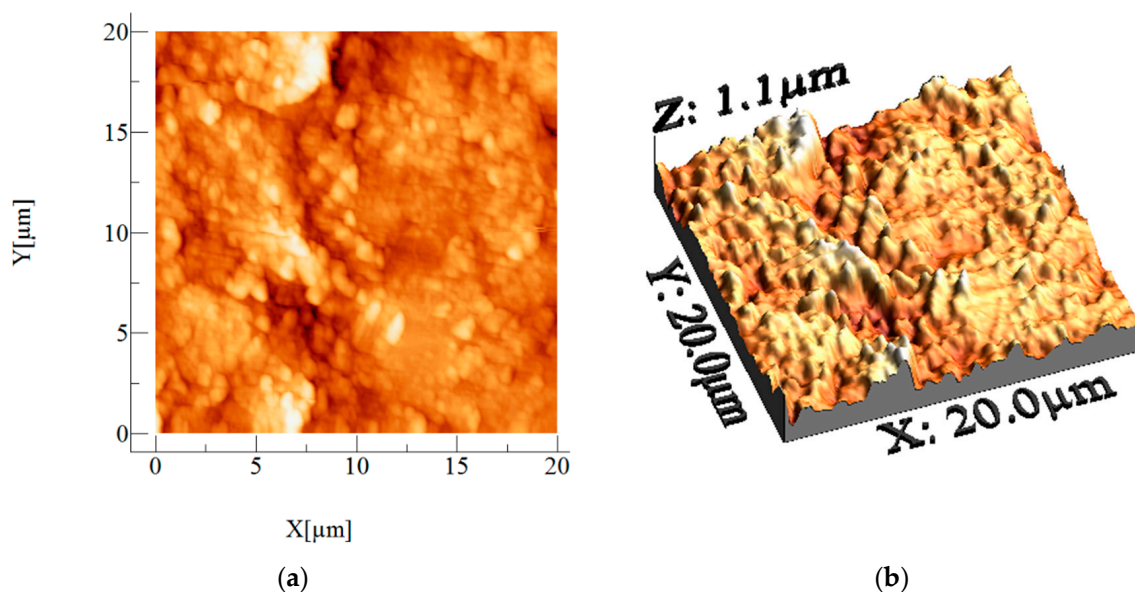
Figure 6. Two- (**a**) and three-dimensional (**b**) images of sample S1.
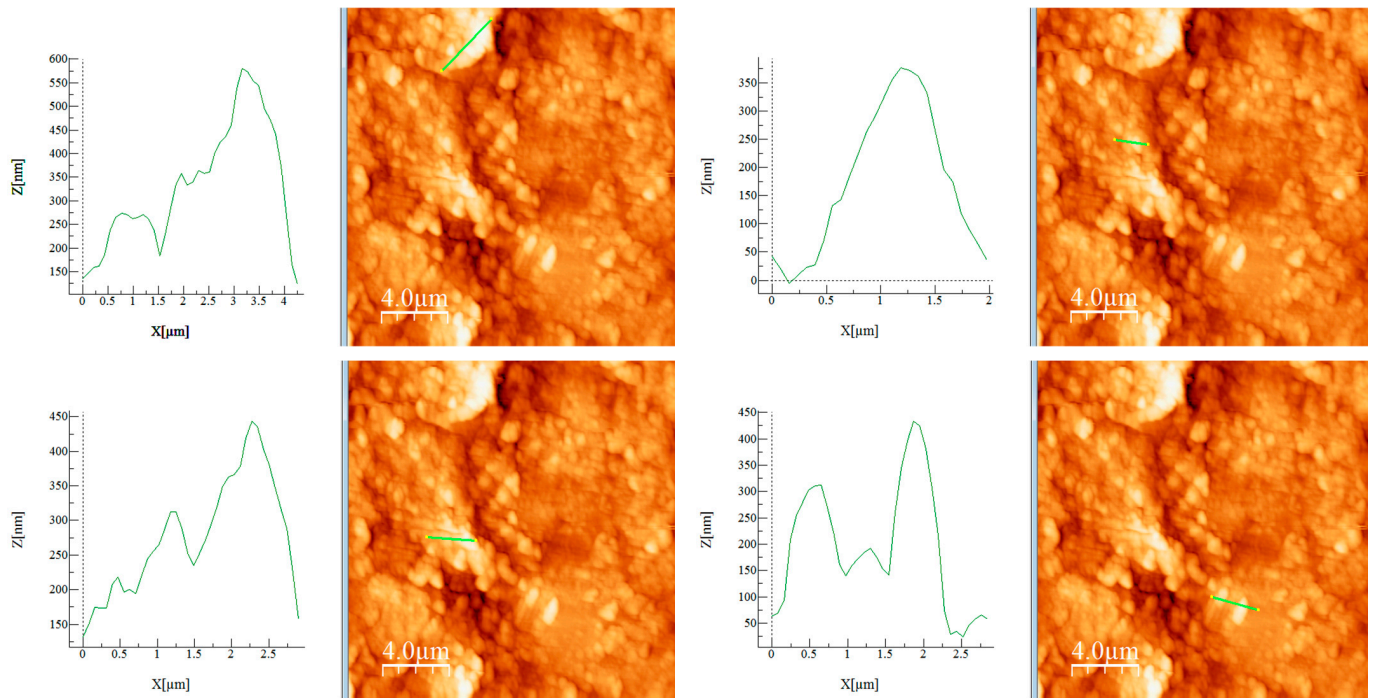
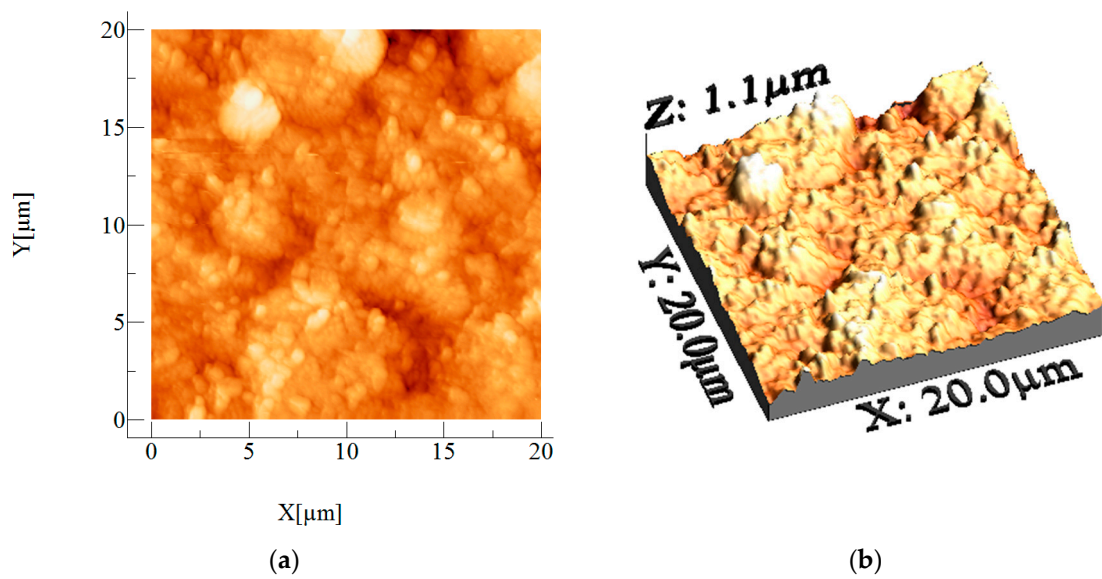**Figure 7.** Surface profile of selected areas of sample S1.

(**a**)

(**b**)

Figure 8. Two- (**a**) and three-dimensional (**b**) images of sample S2.
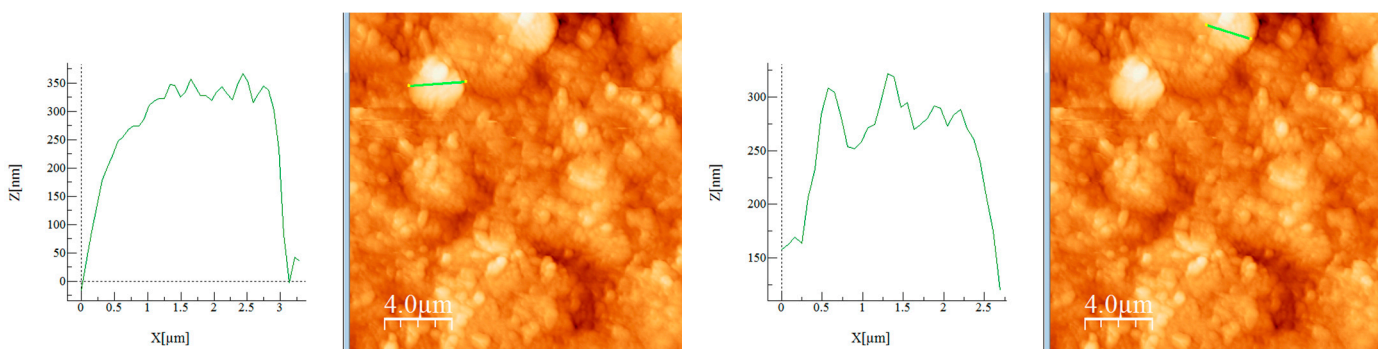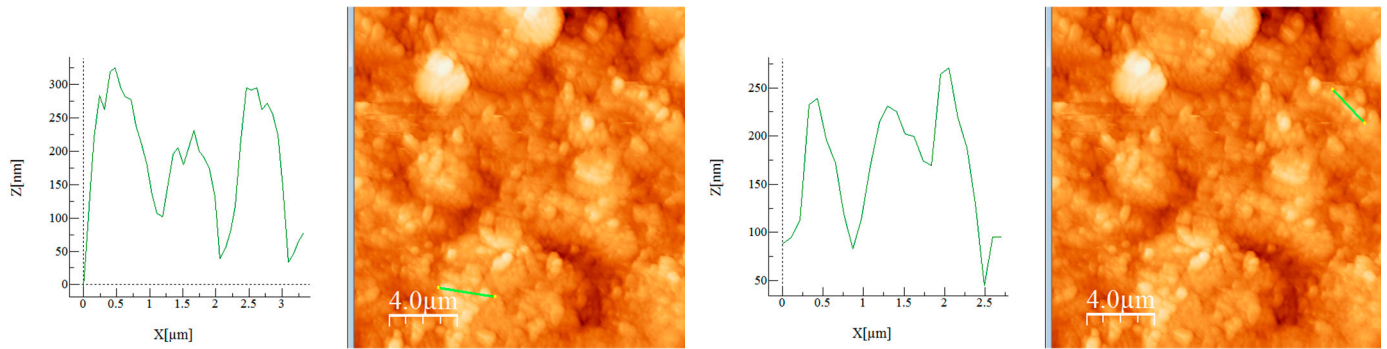

Figure 9. *Cont.*

Figure 9. Surface profile of selected areas of sample S2.

3.6. Degradation of Methyl Orange

The performance of PVP–perovskite composites in terms of MO degradation was evaluated as described in Section 2.4. Accordingly, the representation of the in-time degradation ratio (Figure 10a, Figure 11, Figure 12) was an easy way to visualize and investigate the results. The degradation ratio was calculated as the ratio between the intensity of the MO solution absorbance peak recorded at certain periods (A) during the reaction time and the intensity of the initial absorbance peak (A_0) measured at the wavelengths of 503 nm at pH = 4, 505 nm at pH = 3, and 507 nm at pH = 2. The shift in the absorbance peak on the intensity axis and on the position axis, determined by the variation in pH, is represented in Figure 10b.
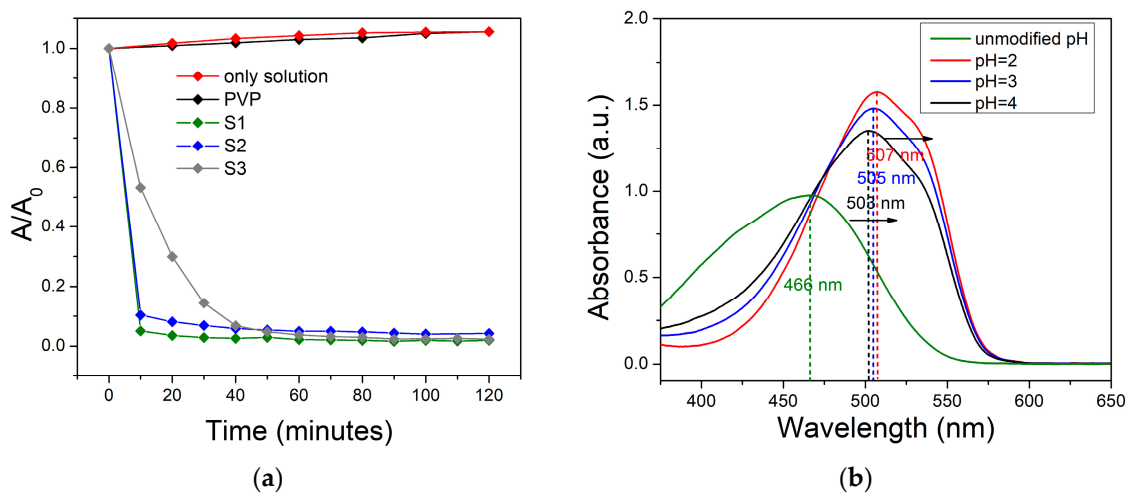

Figure 10. (**a**) Time-dependent degradation ratio (A/A_0) illustrated at pH = 2 for reference test and for each test material (S1, S2, and S3); (**b**) representation of peak shape changes for absorbance of MO solution before pH adjustment and at pH = 2, pH = 3, and pH = 4.

By analyzing the data exhibited in Figure 11, our analysis indicated that the highly acidic condition favored the degradation of the colorant, resulting in almost complete MO elimination at pH = 2 (D_{eff} = 98% for S1, D_{eff} = 96% for S2, and D_{eff} = 98% for S3). Higher values of the suspension pH led to a decrease in discoloration efficiency; each material corresponded to this trend according to the calculation after two hours of reaction, but they displayed different behavior during the reaction.

Therefore, the D_{eff} after two hours of experiment decreased as follows: 98% (pH = 2) > 94% (pH = 3) > 58% (pH = 4) for S1 composite (Figure 12a); 96% (pH = 2) > 94% (pH = 3) > 91% (pH = 4) for S2 composite (Figure 12b); and 98% (pH = 2) > 71% (pH = 3) ≈71% (pH = 4) for S3 composite (Figure 12c).
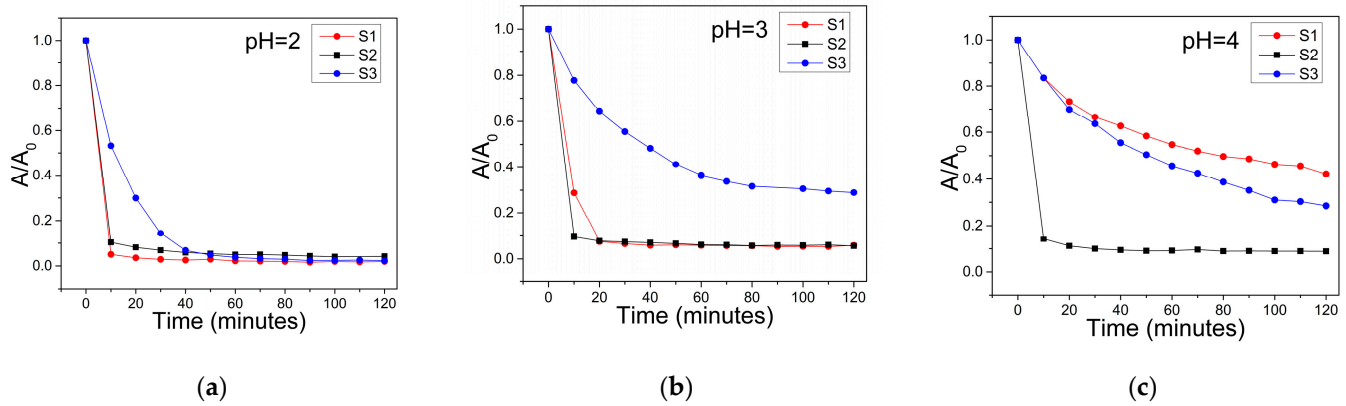
Figure 11. Degradation ratio (A/A_0) vs. time calculated at (**a**) pH = 2, (**b**) pH = 3, and (**c**) pH = 4 for samples S1, S2, and S3.
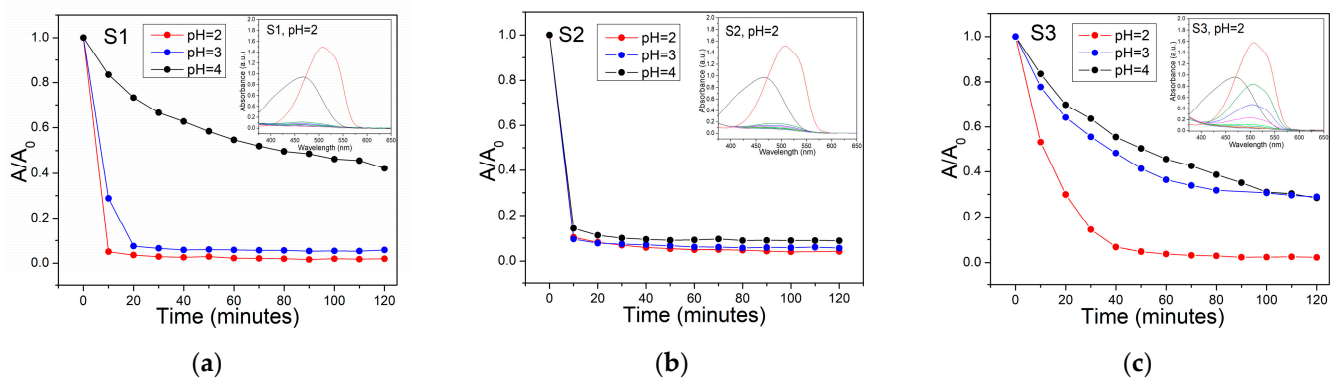

Figure 12. Degradation ratio (A/A_0) vs. time calculated for (**a**) S1, (**b**) S2, and (**c**) S3 in different acidic environments (pH = 2, pH = 3, pH = 4), with inset representing the absorbance peaks of MO solution monitored over two hours at pH = 2 for (**a**) S1 composite, (**b**) S2 composite, and (**c**) S3composite.

In compliance with Figure 10a, these results can be ascribed to the action of perovskite. As has been claimed in other research studies, methyl orange is a stable organic compound that does not degrade without external action [49,50]; in our research work, no MO degradation occurred at pH = 2 in the solution alone or when PVP was added. Overall, the S2 composite appeared to have a better effect on MO degradation due to the fact that MO was mostly degraded in the first 30 min, and slight differences emerged when pH is changed. For the other composites, S2 and S3, the degradation decreased more significantly when the pH increased, for example, in the case of the S1 sample at pH = 4 and the S3 sample at pH = 3 and pH = 4. One more experiment was conducted for an extended period (4 h) using the S3 composite and the same MO and composite concentration under acidic conditions (pH between 2 and 3). UV-VIS spectra were recorded between 200 and 650 nm (Figure 13), and the main objective was to visualize the spectra profiles in the UV domain wherein the peaks correlated with the compounds and molecular structures that did not emit color could be identified. With regard to Figure 13, two primary absorption peaks were found with absorption maxima at 506 nm and 317 nm; they were assigned to the azo chromophore group (-N = N-) and the aromatic ring, respectively [51]. Typically, these peaks appear at maximum absorption wavelengths of 465 nm and 270 nm, but are shifted to the higher wavelength values as a consequence of interaction between the dye and the acid, which results in derived protonated species [51,52].
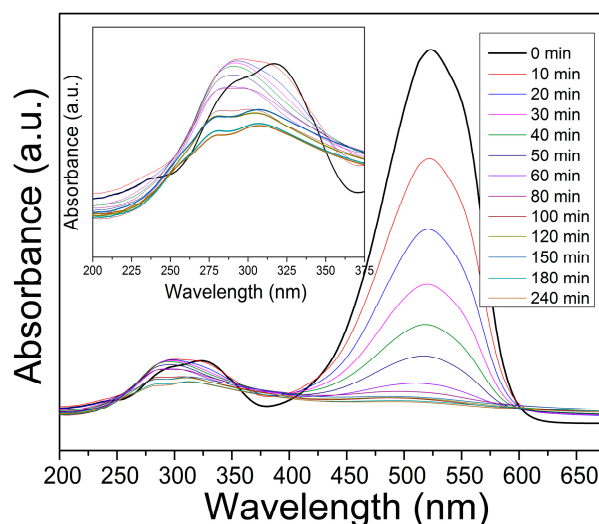
Figure 13. UV-VIS spectra of MO acidic solution monitored for 4 h over the course of MO degradation reaction assisted by the S3 composite; inset: in-time variation in the absorption spectra between 200 and 375 nm.

After carefully analyzing the time-dependent absorption spectra in the UV range (inset of the Figure 13), the analysis indicated that once the reaction started, the initial peak (attributed to the aromatic ring of the MO molecule), marked with black line, experienced a bathochromic shift, and two overlapped peaks emerged and became more defined as the reaction time progressed. These peaks were indicative of transformation that occurred at aromatic ring during the degradation of MO, and the decrease in intensity validated the elimination of the MO compound not only through the disappearance of chromophoric group absorption peak, which resulted in discoloration of the solution, but also through the disappearance of the peak corresponding to the aromatic ring.

The composites showed different operability in the acidic environment: the S1 and S2 samples were destroyed in the acidic MO aqueous solution, whereas the S3 composite could be visually observed in the solution throughout the reaction, which may indicate that the underlying mechanism of MO elimination was particular for the S1 and S2 samples and for the S3 sample, respectively.

The destruction of S1 and S2 PVP–perovskite samples was assumed to result from a dissolution process caused by acidic conditions. It must be mentioned that preliminary tests were carried out at a basic pH, and neither visible destruction of the materials and nor MO degradation activity occurred. Some perovskite materials (e.g., $SrMIrO_6$, where M = Fe and Co, La; $La_xSr_{1-x}MnO_3$, $La_xSr_{1-x}CoO_3$, $LaMnO_3$, $La_xSr_{1-x}Co_yFe_{1-y}O_3$) have been documented to be susceptible to dissolution by acid action, which alters the surface structural properties of the materials and enables the formation of other species of the A and/or B site cations with the aim of improving catalytic activity [53–57]. Rekavandi et al. [49] carried out an investigation to degrade MO over $LaMnO_3$ nanoparticles synthesized via the sol–gel method in a 20 mL aqueous solution with a 6.5 ppm concentration. They conducted various tests, for which parameters such as the catalyst amount, pH of the reaction environment, temperature, and the effect of dark conditions and solar radiation were assessed. Based on their analysis of the pH_{pzc} parameter, the surface charge of $LaMnO_3$ materials was positive at an acidic pH, and in this way, the adsorption and degradation reaction of negatively charged dyes was promoted. Moreover, they obtained no MO degradation at pH values of 6.7 and 10.5 [49]. The zeta potential parameter is widely assessed for the determination of the surface charges of solid materials, an important piece of information in adsorption and catalytic processes that can be used to establish an experimental configuration where

the materials are active for the predetermined application. Based on the zeta potential analysis, the value of pH for which the surface charge of the material was found to be zero [58]. The charge of the surface was positive below the pH of zero charge potential and negative above this value. The charge of the pollutant dissolved in the environment should have the opposite charge in order to be adsorbed on the surface of the catalyst. Perovskite materials display variations in zeta potential correlated with the pH value. Hasanly found out that the zero charge of $LaMnO_3$ material is in the pH range between 1 and 2 [59]. Christensen et al. claimed that $LaCoO_{3-\delta}$ and $LaCo_{0.2}Ni_{0.8}O_{3-\delta}$ are positively charged in acidic solution and have zero charge in the pH range of 4.35–6.10. They conducted catalytic experiments at a pH of 2 with Rhodamine B, which was negatively charged at low pH values [60]. The $LaFeO_3$–La_2O_3 perovskite material synthesized by Li et al. was positively charged when dispersed in water and presented good adsorption properties for methyl orange [61]. In the study carried out by Wang et al., it was found that the point of zero charge of the perovskite was around the pH value of 4.1 [62].

The use of acidic conditions favored the catalytic degradation of MO by the PVP–perovskite composites developed in the current research and by other lanthanum manganite perovskites, as stated in previous work and in other research studies [10,49,63,64]. Therefore, an acidic pH of the suspension can be presumed to have a double function: firstly, to mediate the adsorption and heterogeneous catalytic degradation of MO, a process that can be attributed to the S3 composite by modifying the surface electric charge and consequently inducing electrostatic attraction between the composite and anionic dye; and secondly, to assist in the dissolution of the S1 and S2 perovskite composites into soluble reactive species of the La and/or Mn sites (possibly lanthanum or manganese oxides) that will further degrade MO through a homogenous reaction [49,54,55,65,66]. However, the dissolution process cannot be excluded for the S3 composite. The degradation of MO assisted by the composites, which occurs homogeneously or heterogeneously, can be related to the degradation mechanisms involving the reactive radical species that sustain the degradation reactions up to the demineralization of the pollutant [67,68]. Redox reactions occur at the surface of the material when they are not dissolved, or when the available metal ions in the solution generate electrons that react with the dissolved species in the solution [67,69,70]. Electrons can participate in the formation of oxygen free radical species (superoxide radicals and hydroxyl radicals) that propagate the decomposition of colored organic pollutants via the breakdown of chromophoric groups and aromatic rings [67]. According to the literature, the degradation of methyl orange may involve the cleavage of azo chromophoric bonds; the formation of N-demethylation intermediates, which are further decomposed in aromatic products (e.g., benzenesulfonate, 4-amino benzaldehyde, benzene etc.); the destruction of aromatic by-products into simpler products, such as carboxylic acids and aldehydes, as well as into demineralization products, such as H_2O and CO_2 [68].

The Ag-doped $LaMnO_3$ nanoparticles were synthesized in a previous study, as stated in the Materials and Methods section, and were tested for catalytic degradation of MO using an acidic environment under dark conditions and solar irradiation, then compared with Pd-, Y-doped, and undoped $LaMnO_3$ [10]. In the current research, we continued to study the Ag-doped $LaMnO_3$ blended with PVP and developed new materials, the S1, S2, and S3 composites, through different procedures and tested them as described above for the degradation of MO using conditions adjusted to the composites. The novelty of this study is in the development of more complex materials, i.e., the new composites, and in finding potential applications, such as catalysis. The findings related to the morphology emphasize the presence of perovskite in the PVP matrix for the S3 sample. Concerning the application results, an acidic environment was suitable for both perovskite materials and PVP–perovskite composites, but the perovskite materials had the advantage of showing

no visible destruction during the catalytic experiments. Stability is an issue for the PVP–perovskite composites in the given conditions, but on the other hand, despite the changes in the composite materials during the degradation experiments, up to 98% of the pollutant, MO, was removed at the lower pH. The progress of the composites validated by the spectroscopic, structural, and morphological analyses presented in this study can serve as a starting point for further investigation and development of their synthesis, properties, and application.

4. Conclusions

In this work, perovskite–polymer composites based on polyvinylpyrrolidone and 1% Ag-doped LaMnO$_3$ were prepared by three different methods. The samples were physicochemically characterized, and their MO degradation performance was evaluated. Raman and FT-IR spectroscopic measurements displayed bands specific to both the polymer and perovskite materials' molecular groups. In conjunction with morphological characterization, the formation of PVP/Ag-LaMnO$_3$ blends with different morphology configurations for each sample was confirmed. Herein, SEM images of S$_3$ samples show that the LaMnO$_3$ nanoparticles were distributed on the PVP surface. Based on the XRD analysis, it was found that the perovskite maintained the crystalline structure in the new composite materials, which is of interest for the catalysis application. The results regarding the MO degradation are closely correlated to the preparation procedure of PVP–perovskite composites. So far, by analyzing the investigation conducted in this research, S1 and S2 samples seem to be very similar from morphological and compositional points of view. It can be attested that the microwave-assisted synthesis provided a more efficient composite, S2, for degradation of MO, but both the S1 and S2 samples had the main drawback of being unstable in solutions with acidic pH values. For that reason, we are more inclined to state that the S3 sample is more suitable for catalytic applications due to its better stability, which was ascribed to the PVP transformation in the thermal treatment and comparable MO degradation efficiency. Moreover, for all samples (S1, S2, S3), it can be concluded that the perovskite was the active material for pollutant degradation, whereas the PVP served as support for encompassing the Ag–perovskite materials. With regard to these results and to the best of our knowledge, we report for the first time the synthesis of PVP-Ag-based perovskite materials which are capable of MO elimination from the aqueous environment, with positive outcomes related to the preparation method, morphology, and applications for pollutant destruction.

References

1. Briffa, J.; Sinagra, E.; Blundell, R. Heavy metal pollution in the environment and their toxicological effects on humans. *Heliyon* **2020**, *6*, e04691. [CrossRef] [PubMed]

2. Garba, Z.N.; Zhou, W.; Zhang, M.; Yuan, Z. A review on the preparation, characterization and potential application of perovskites as adsorbents for wastewater treatment. *Chemosphere* **2020**, *244*, 125474. [CrossRef]

3. Zhang, W.; Liu, Z.; Chen, P.; Zhou, G.; Liu, Z.; Xu, Y. Preparation of Supported Perovskite Catalyst to Purify Membrane Concentrate of Coal Chemical Wastewater in UV-Catalytic Wet Hydrogen Peroxide Oxidation System. *Int. J. Environ. Res. Public Health* **2021**, *18*, 4906. [CrossRef] [PubMed]

4. Mukherjee, J.; Lodh, B.K.; Sharma, R.; Mahata, N.; Shah, M.P.; Mandal, S.; Ghanta, S.; Bhunia, B. Advanced oxidation process for the treatment of industrial wastewater: A review on strategies, mechanisms, bottlenecks and prospects. *Chemosphere* **2023**, *345*, 140473. [CrossRef] [PubMed]

5. Dhariwal, S.; Mittal, M. Wastewater treatment with perovskite-based photocatalysts: Environmental sustainability from a green perspective. *Mater. Today Proc.* **2023**, *in press*. [CrossRef]

6. Borah, P.; Kumar, M.; Devi, P. Recent trends in the detection and degradation of organic pollutants. In *Abatement of Environmental Pollutants*, 1st ed.; Singh, P., Kumar, A., Borthakur, A., Eds.; Elsevier: Amsterdam, The Netherlands, 2020; pp. 67–79. [CrossRef]

7. Ibrahim, I.; Belessiotis, G.V.; Ahmed, A.; Boedicker, J.R.; Eliwa, E.M.; Moneam, I.A.; Elseman, A.M.; Mohamed, G.G.; Mohamed, M.M.; Salama, T.M. Water treatment by perovskite materials and their applications: A comprehensive review. *J. Ind. Eng. Chem.* **2024**, *in press*. [CrossRef]

8. Mehdizadeh, P.; Amiri, O.; Rashki, S.; Salavati-Niasari, M.; Salimian, M.; Foong, L.K. Effective removal of organic pollution by using sonochemical prepared $LaFeO_3$ perovskite under visible light. *Ultrason. Sonochem.* **2020**, *61*, 104848. [CrossRef]

9. Arif, A.; Aziz, F.; Sokri, M.N.M.; Sahimi, M.S.; Yahya, N.; Jaafar, J.; Salleh, W.N.W.; Yusof, N.; Ismail, A.F. Photocatalytic degradation of phenol by $LaFeO_3$ nanocrystalline synthesized by gel combustion method via citric acid route. *SN Appl. Sci.* **2019**, *1*, 91. [CrossRef]

10. Sfirloaga, P.; Ivanovici, M.-G.; Poienar, M.; Ianasi, C.; Vlazan, P. Investigation of Catalytic and Photocatalytic Degradation of Methyl Orange Using Doped $LaMnO_3$ Compounds. *Processes* **2022**, *10*, 2688. [CrossRef]

11. Dumitru, R.; Ianculescu, A.; Păcurariu, C.; Lupa, L.; Pop, A.; Vasile, B.; Surdu, A.; Manea, F. $BiFeO_3$-synthesis, characterization and its photocatalytic activity towards doxorubicin degradation from water. *Ceram. Int.* **2019**, *45*, 2789–2802. [CrossRef]

12. Huerta-Flores, A.M.; Sánchez-Martínez, D.; del Rocío Hernández-Romero, M.; Zarazúa-Morín, M.E.; Torres-Martínez, L.M. Visible-light-driven $BaBiO_3$ perovskite photocatalysts: Effect of physicochemical properties on thephotoactivity towards water splitting and the removal of rhodamine B from aqueous systems. *J. Photochem. Photobiol. A Chem.* **2019**, *368*, 70–77. [CrossRef]

13. Safari, S.; Ahmadian, S.M.S.; Amani-Ghadim, A.R. Visible lightphotocatalytic activity enhancing of $MTiO_3$ perovskites by M cation (M = Co, Cu, and Ni) substitution and Gadolinium doping. *J. Photochem. Photobiol. A Chem.* **2020**, *394*, 112461. [CrossRef]

14. Jiang, J.; Jia, Y.; Wang, Y.; Chong, R.; Xu, L.; Liu, X. Insight into efficientphotocatalytic elimination of tetracycline over $SrTiO_3$(La, Cr) under visible light irradiation: The relationship of doping and performance. *Appl. Surf. Sci.* **2019**, *486*, 93–101. [CrossRef]

15. Di, J.; Zhong, M.; Wang, Y. Polyvinylpyrrolidone/polyvinyl alcohol blends modification on light absorbing layer to improve the efficiency and stability of perovskite solar cells. *Mater. Sci. Semicond. Process.* **2021**, *133*, 105941. [CrossRef]

16. Kumar, A.; Schuerings, C.; Kumar, S.; Kumar, A.; Krishnan, V. Perovskite-structured $CaTiO_3$ coupled with g-C_3N_4 as a heterojunction photocatalyst for organic pollutant degradation. *Beilstein J. Nanotechnol.* **2018**, *9*, 671–685. [CrossRef] [PubMed]

17. Venditto, V.; Vaiano, V.; Sacco, O. Monolithic Porous Organic Polymer-Photocatalyst Composites for Applications in Catalysis. *ChemCatChem* **2024**, *16*, e202301118. [CrossRef]

18. Bathula, C.; Naik, S.; Jana, A.; Palem, R.R.; Singh, A.N.; Hatshan, M.R.; Mane, S.D.; Kim, H.S. Polymer Backbone Stabilized Methylammonium Lead Bromide Perovskite Nano Islands. *Nanomaterials* **2023**, *13*, 2750. [CrossRef] [PubMed]

19. Samu, G.F.; Scheidt, R.A.; Kamat, P.V.; Janáky, C. Electrochemistry and Spectroelectrochemistry of Lead Halide Perovskite Films: Materials Science Aspects and Boundary Conditions. *Chem. Mater.* **2018**, *30*, 561–569. [CrossRef] [PubMed]

20. Mollick, S.; Mandal, T.N.; Jana, A.; Fajal, S.; Desai, A.V.; Ghosh, S.K. Ultrastable Luminescent Hybrid Bromide Perovskite@MOF Nanocomposites for the Degradation of Organic Pollutants in Water. *ACS Appl. Nano Mater.* **2019**, *2*, 1333–1340. [CrossRef]

21. Xian, T.; Yang, H.; Di, L.J.; Dai, J.F. Enhanced photocatalytic activity of $BaTiO_3$@g-C3N4 for the degradation of methyl orange under simulated sunlight irradiation. *J. Alloys Compd.* **2015**, *622*, 1098–1104. [CrossRef]

22. Leong, K.H.; Tan, Z.Z.; Sim, L.C.; Saravanan, P.; Bahnemann, D.; Jang, M. Symbiotic Interaction of Amalgamated Photocatalysts with Improved Day Light Utilisation and Charge Separation. *ChemistrySelect.* **2017**, *2*, 84–89. [CrossRef]

23. Brahmi, C.; Benltifa, M.; Vaulot, C.; Michelin, L.; Dumur, F.; Airoudj, A.; Morlet-Savary, F.; Raveau, B.; Bousselmi, L.; Lalevée, J. New hybrid perovskites/polymer composites for the photodegradation of organic dyes. *Eur. Polym. J.* **2021**, *157*, 110641. [CrossRef]

24. Koczkur, K.M.; Mourdikoudis, S.; Polavarapu, L.; Skrabalak, S.E. Polyvinylpyrrolidone (PVP) in nanoparticle synthesis. *Dalton Trans.* **2015**, *44*, 17883. [CrossRef]

25. Wang, Z.; Tang, Y.; Ai, L.; Liu, M.; Wang, Y. Polymer-Based Immobilized FePMo$_{12}$O$_{40}$@PVP Composite Materials for Photocatalytic RhB Degradation. *Inorganics* **2024**, *12*, 144. [CrossRef]

26. Deng, Z.; Li, Y.; Zheng, X.; Guo, Y. Photocatalytic activity evaluation of polyvinylpyrrolidone K30 assisted synthesis of 1D oxygen-vacancy-rich Bi5O7BrxI1-x nanorod solid solution. *J. Hazard. Mater.* **2024**, *465*, 133361. [CrossRef] [PubMed]

27. Wen, J.; Du, X.; Hua, F.; Gu, Y.; Li, M.; Tang, T. PVP Passivatedδ-CsPbI$_3$: Vacancy Induced Visible-Light Absorption and Efficient Photocatalysis. *Molecules* **2024**, *29*, 1670. [CrossRef]

28. Memon, K.; Memon, R.; Khalid, A.; Al-Anzi, B.S.; Uddin, S.; Sherazi, S.T.H.; Chandio, A.; Talpur, F.N.; Latif, A.A.; Liaqat, I. Synthesis of PVP-capped trimetallic nanoparticles and their efficient catalytic degradation of organic dyes. *RSC Adv.* **2023**, *13*, 29270–29282. [CrossRef]

29. Qing, Q.; Chen, S.-Y.; Hu, S.-Z.; Li, L.; Huang, T.; Zhang, N.; Wang, Y. Highly Efficient Photocatalytic Degradation of Organic Pollutants Using a Polyvinylidene Fluoride/Polyvinylpyrrolidone-Cuprous Oxide Composite Membrane. *Langmuir* **2024**, *40*, 1447–1460. [CrossRef]

30. Shakiyeva, T.V.; Dossumova, B.T.; Sassykova, L.R.; Ilmuratova, M.S.; Dzhatkambayeva, U.N.; Abildin, T.S. Study of the Oxidation of Phenol in the Presence of a Magnetic Composite Catalyst CoFe$_2$O$_4$/Polyvinylpyrrolidone. *Appl. Sci.* **2024**, *14*, 8907. [CrossRef]

31. Li, H.; Wang, N.; Li, H.; Ren, Z.; Ma, W.; Li, J.; Du, Y.; Xu, Q. Polyvinylpyrrolidone-induced size-dependent catalytic behavior of Fe sites on N-doped carbon substrate and mechanism conversion in Fenton-like oxidation reaction. *Appl. Catal. B-Environ.* **2024**, *341*, 123323. [CrossRef]

32. Baganizi, D.R.; Nyairo, E.; Duncan, S.A.; Singh, S.R.; Dennis, V.A. Interleukin-10 Conjugation to Carboxylated PVP-Coated Silver Nanoparticles for Improved Stability and Therapeutic Efficacy. *Nanomaterials* **2017**, *7*, 165. [CrossRef] [PubMed]

33. Mireles, L.K.; Wu, M.-R.; Saadeh, N.; Yahia, L.; Sacher, E. Physicochemical Characterization of Polyvinyl Pyrrolidone: A Tale of Two Polyvinyl Pyrrolidones. *ACS Omega* **2020**, *5*, 30461–30467. [CrossRef]

34. Safo, I.A.; Werheid, M.; Dosche, C.; Oezaslan, M. The role of polyvinylpyrrolidone (PVP) as a capping and structure-directing agent in the formation of Pt nanocubes. *Nanoscale Adv.* **2019**, *1*, 3095. [CrossRef]

35. Song, Y.-J.; Wang, M.; Zhang, Y.-Y.; Wu, J.-Y.; Zhang, T. Investigation of the role of the molecular weight of polyvinyl pyrrolidone in the shape control of high-yield silver nanospheres and nanowires. *Nanoscale Res. Lett.* **2014**, *9*, 17. [CrossRef]

36. Kim, J.H.; Min, B.R.; Kim, C.K.; Won, J.; Kang, Y.S. Spectroscopic Interpretation of Silver Ion Complexation with Propylene in Silver Polymer Electrolytes. *J. Phys. Chem. B* **2002**, *106*, 2786–2790. [CrossRef]

37. Bryaskova, R.; Daniela Pencheva, D.; Nikolov, S.; Kantardjiev, T. Synthesis and comparative study on the antimicrobial activity of hybrid materials based on silver nanoparticles (AgNps) stabilized by polyvinylpyrrolidone (PVP). *J. Chem. Biol.* **2011**, *4*, 185–191. [CrossRef]

38. Yoshida, M.; Prasad, P.N. Fabrication of channel waveguides from sol-gel-processed polyvinylpyrrolidone/SiO$_2$ composite materials. *Appl. Opt.* **1996**, *35*, 1500–1506. [CrossRef] [PubMed]

39. Borodko, Y.; Habas, S.E.; Koebel, M.; Yang, P.; Frei, H.; Somorjai, G.A. Probing the interaction of poly(vinylpyrrolidone) with platinum nanocrystals by UV-Raman and FTIR. *J. Phys. Chem. B* **2006**, *110*, 23052–23059. [CrossRef]

40. Borodko, Y.; Lee, H.S.; Joo, S.H.; Zhang, Y.; Somorjai, G. Spectroscopic Study of the Thermal Degradation of PVP-Capped Rh and Pt Nanoparticles in H$_2$ and O$_2$ Environments. *J. Phys. Chem. C* **2010**, *114*, 1117–1126. [CrossRef]

41. Behera, M.; Ram, S. Inquiring the mechanism of formation, encapsulation, and stabilization of gold nanoparticles by poly(vinyl pyrrolidone) molecules in 1-butanol. *Appl. Nanosci.* **2014**, *4*, 247–254. [CrossRef]

42. Mao, H.; Feng, J.; Ma, X.; Wu, C.; Zhao, X. One-dimensional silver nanowires synthesized by self-seeding polyol process. *J. Nanoparticle Res.* **2012**, *14*, 887. [CrossRef]

43. Martín-Carrón, L.; de Andrés, A. Melting of the cooperative Jahn-Teller distortion in LaMnO$_3$ single crystal studied by Raman spectroscopy. *Eur. Phys. J. B* **2001**, *22*, 11–16. [CrossRef]

44. Sudewi, S.; Chabib, L.; Zulfajri, M.; Gedda, G.; Huang, G.G. Polyvinylpyrrolidone passivated fluorescent Iron oxide quantum dots for turn-off detection of tetracycline in biological fluids. *J. Food Drug Anal.* **2023**, *31*, 12. [CrossRef]

45. Wahadoszamen, M.; Rahaman, A.; Hoque, N.M.R.; Talukder, A.I.; Abedin, K.M.; Haider, A.F.M.Y. Laser Raman Spectroscopy with Different Excitation Sources and Extension to Surface Enhanced Raman Spectroscopy. *J. Spectrosc.* **2015**, *2015*, 895317. [CrossRef]

46. Tuschel, D. Selecting an Excitation Wavelength for Raman Spectroscopy. *Spectroscopy* **2016**, *31*, 14–23.

47. Berthou, H.; Faure, C.; Hänni, W.; Perret, A. Morphology and Raman spectra of diamond films grown with a plasma torch. *Diam. Relat. Mater.* **1999**, *8*, 636–639. [CrossRef]

48. Rahimi, M.; Aslani, M.R.; Rezai, B. Influence of surface roughness on flotation kinetics of quartz. *J. Cent. South Univ.* **2012**, *19*, 1206–1211. [CrossRef]

49. Rekavandi, N.; Malekzadeh, A.; Ghiasi, E. Methyl orange degradation over nano-LaMnO$_3$ as a green catalyst under the mild conditions. *Nanochemistry Res.* **2019**, *4*, 1–10. [CrossRef]

50. Dvininov, E.; Joshi, U.A.; Darwent, J.R.; Claridge, J.B.; Xu, Z.; Rosseinsky, M.J. Room temperature oxidation of methyl orange and methanol over Pt–HCa$_2$ Nb$_3$ O$_{10}$ and Pt–WO$_3$ catalysts without light. *Chem. Commun.* **2011**, *47*, 881–883. [CrossRef] [PubMed]

51. Tasaki, T.; Wada, T.; Fujimoto, K.; Kai, S.; Ohe, K.; Oshima, T.; Baba, Y.; Kukizaki, M. Degradation of methyl orange using short-wavelength UV irradiation with oxygen microbubbles. *J. Hazard. Mater.* **2009**, *162*, 1103–1110. [CrossRef]

52. De Vylder, M.; De Keukeleire, D. Aggregation of Methyl Orange in Aqueous Acidic Solution. *Bull. Sociétés Chim. Belg.* **1978**, *87*, 9–13. [CrossRef]

53. Zhang, R.; Dubouis, N.; Osman, M.B.; Yin, W.; Sougrati, M.T.; Corte, D.A.D.; Giaume, D.; Grimaud, A. A Dissolution/Precipitation Equilibrium on the Surface of Iridium-Based Perovskites Controls Their Activity as Oxygen Evolution Reaction Catalysts in Acidic Media. *Angew. Chem. Int. Ed.* **2019**, *58*, 4571–4575. [CrossRef] [PubMed]

54. Si, W.; Wang, Y.; Peng, Y.; Li, J. Selective Dissolution of A-Site Cations in ABO_3 Perovskites: A New Path to High-Performance Catalysts. *Angew. Chem. Int. Ed.* **2015**, *54*, 7954–7957. [CrossRef] [PubMed]

55. Peng, Y.; Si, W.; Li, J.; Crittenden, J.; Hao, J. Experimental and DFT studies on Sr-doped $LaMnO_3$ catalysts for NO_x storage and reduction. *Catal. Sci. Technol.* **2015**, *5*, 2478–2485. [CrossRef]

56. Peng, Y.; Si, W.; Luo, J.; Su, W.; Chang, H.; Li, J.; Hao, J.; Crittenden, J. Surface Tuning of $La_{0.5}Sr_{0.5}CoO_3$ Perovskite Catalysts by Acetic Acid for NO_x Storage and Reduction. *Environ. Sci. Technol.* **2016**, *50*, 6442–6448. [CrossRef]

57. Guo, W.; Cui, L.; Xu, H.; Gong, C. Selective dissolution of A-site cations of $La_{0.6}Sr_{0.4}Co_{0.8}Fe_{0.2}O_3$ perovskite catalysts to enhance the oxygen evolution reaction. *Appl. Surf. Sci.* **2020**, *529*, 147165. [CrossRef]

58. Ghattavi, S.; Nezamzadeh-Ejhieh, A. GC-MASS detection of methyl orange degradation intermediates by $AgBr/g-C_3N_4$: Experimental design, bandgap study, and characterization of the catalyst. *Int. J. Hydrog. Energy* **2020**, *45*, 24636–24656. [CrossRef]

59. Hasanli, H. *Synthesis of Graphene-Templated Metal Oxide Catalyst Hybrid Structures for a New Generation of Cathode Material*; M1 Internship report, Chimie ParisTech; Université PSL: Paris, France, 12 July 2024. [CrossRef]

60. Christensen, B.H.; Deganello, F.; La Parola, V.; Jørgensen, M.K.; Boffa, V.; Østergaard, M.B. Thermocatalytic Performance of $LaCo_{1-x}Ni_xO_{3-\delta}$ Perovskites in the Degradation of Rhodamine B. *Catalysts* **2023**, *13*, 325. [CrossRef]

61. Li, J.; Miao, J.; Duan, X.; Dai, J.; Liu, Q.; Wang, S.; Zhou, W.; Shao, Z. Fine-Tuning Surface Properties of Perovskites via Nanocompositing with Inert Oxide toward Developing Superior Catalysts for Advanced Oxidation. *Adv. Funct. Mater.* **2018**, *28*, 1804654. [CrossRef]

62. Wang, W.; Zhu, Y.; Zhang, S.; Deng, J.; Huang, Y.; Yan, W. Flotation Behaviors of Perovskite, Titanaugite, and Magnesium Aluminate Spinel Using Octyl Hydroxamic Acid as the Collector. *Minerals* **2017**, *7*, 134. [CrossRef]

63. Ghiasi, M.; Malekzadeh, A. Solar photocatalytic degradation of methyl orange over $La_{0.7}Sr_{0.3}MnO_3$ nano-perovskite. *Sep. Purif. Technol.* **2014**, *134*, 12–19. [CrossRef]

64. Shaterian, M.; Enhessari, M.; Rabbani, D.; Asghari, M.; Salavati-Niasari, M. Synthesis, characterization and photocatalytic activity of $LaMnO_3$ nanoparticles. *Appl. Surf. Sci.* **2014**, *318*, 213–217. [CrossRef]

65. Ikram, M.; Abid, N.; Haider, A.; Ul-Hamid, A.; Haider, J.; Shahzadi, A.; Nabgan, W.; Goumri-Said, S.; Butt, A.R.; Kanoun, M.B. Toward efficient dye degradation and the bactericidal behavior of Mo-doped La_2O_3 nanostructures. *Nanoscale Adv.* **2022**, *4*, 926–942. [CrossRef] [PubMed]

66. Li, H.; Fu, B.; Huang, H.; Wu, S.; Ge, J.; Zhang, J.; Li, F.; Qu, P. Catalytic degradation of organic pollutants by manganese oxides: A comprehensive review. *Environ. Pollut. Bioavailab.* **2022**, *34*, 395–406. [CrossRef]

67. Cerón-Urbano, L.; Aguilar, C.J.; Diosa, J.E.; Mosquera-Vargas, E. Nanoparticles of the Perovskite-Structure $CaTiO_3$ System: The Synthesis, Characterization, and Evaluation of Its Photocatalytic Capacity to Degrade Emerging Pollutants. *Nanomaterials* **2023**, *13*, 2967. [CrossRef] [PubMed]

68. Feng, Q.; Tang, Y.; Wang, K.; Wu, C.; Huang, X. Study on the degradation of methyl orange by UV-acetylacetone advanced oxidation system. *Desalin. Water Treat.* **2025**, *321*, 100928. [CrossRef]

69. Verduzco, L.E.; Garcia-Díaz, R.; Martinez, A.I.; Almanza Salgado, R.; Méndez-Arriaga, F.; Lozano-Morales, S.A.; Avendaño-Alejo, M.; Padmasree, K.P. Degradation efficiency of methyl orange dye by $La_{0.5}Sr_{0.5}CoO_3$ perovskite oxide under dark and UV irradiated conditions. *Dye. Pigment.* **2020**, *183*, 108743. [CrossRef]

70. Chatt, J.; Halpern, J. Homogeneous Catalysis by Metal Ions and Complexes. In *Catalysis Progress in Research*; Basolo, F., Burwell, R.L., Eds.; Springer US: Boston, MA, USA, 1973; pp. 107–129. [CrossRef]